

June 13, 2022

# Experiences from the Commissioning and First Physics Run of the Fermilab Muon g-2 Experiment

RAN HONG

ON BEHALF OF THE MUON G-2 COLLABORATION

*Argonne National Laboratory, High Energy Physics Division  
9700 S Cass Ave, IL 60439, USA*

The Muon g-2 Experiment (E989) at Fermilab is seeking to measure the anomalous magnetic moment of muon ( $a_\mu$ ) with a precision of 140 parts-per-billion (ppb) and aiming to resolve the discrepancy between the E821 measurement and the Standard Model calculation of  $a_\mu$ . In E989, the muon beam is stored in a ring magnet. The anomalous spin precession frequency  $\omega_a$  is measured by counting decay positrons in 24 calorimeters, and the magnetic field is measured by nuclear magnetic resonance (NMR) probes. Improvements in this experiment with respect to its predecessor and the progress achieved in the commissioning run and the first physics run, Run-1, are presented.

PRESENTED AT

Thirteenth Conference on the Intersections of Particle and  
Nuclear Physics  
Palm Springs, CA, USA, May 29 – June 3, 2018

# 1 Introduction

The  $g$ -factor of a particle is the ratio of its magnetic moment (measured in  $\mu_B \equiv q/2m$ ) and spin, and for spin-1/2 elementary particles  $g = 2$  if no quantum corrections are taken into account. Due to quantum corrections, the  $g$ -factor deviates from 2 [1], and the lepton magnetic anomaly  $a = (g-2)/2$  describes the amount of the deviation. The part-per-billion level agreement between the measured electron anomaly  $a_e$  and the prediction of it based on the Standard-Model (SM) physics has been a benchmark for the validity of quantum electrodynamics (QED) [2]. For muons,  $a_\mu$  was measured (in experiment E821) with a precision of 540 ppb at Brookhaven National Lab [3]. In 2006, the final result of E821 was different from the SM prediction by 2.5 standard deviations. This difference motivated the physics community to search for mechanisms beyond the SM [4] that can explain the difference, as well as more accurate calculations of the contributions to  $a_\mu$  from the known physics within the SM [5]. Recently there have been great progresses in calculating the contributions from hadronic vacuum polarization (HVP) diagrams and hadronic light-by-light (HLbL) diagrams. The uncertainty on the HVP contribution was improved by using the dispersion-relation approach [6] with more recent experimental data [7], while the HLbL contribution was better estimated using Lattice-QCD [8]. Recently Lattice-QCD calculations for HVP and dispersion-relation approach for HLbL are also developed [9, 10, 11]. Recent results [5] are shown in Figure 1, and the difference between the theoretical calculations and the previous measured value persists.

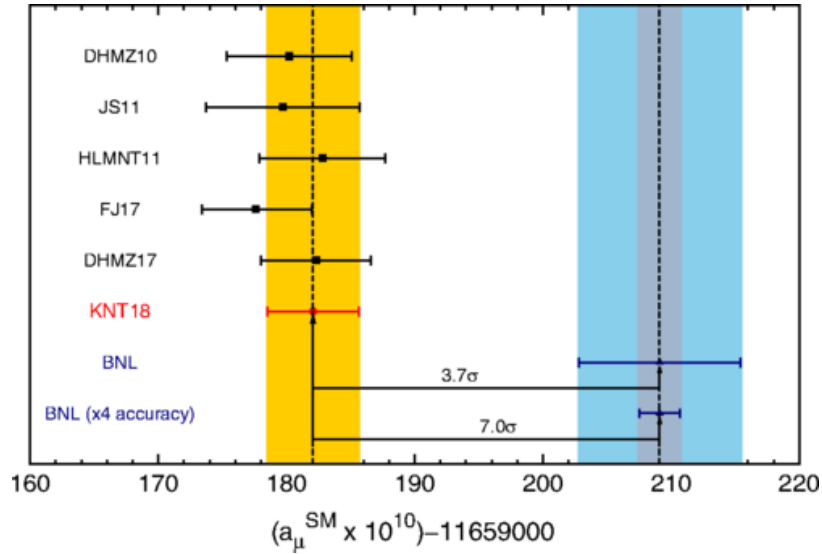


Figure 1: Recent theoretical calculations of the anomalous magnetic moment of muon  $a_\mu$  in the Standard Model. The result of the experiment E821 and the projected uncertainty of E989 are also shown. This figure was originally presented in Reference [5].

The Muon g-2 Experiment at Fermilab (E989) [12] is aiming at reducing the experimental uncertainty down to 140 ppb, a factor of 4 improvement from E821. The new result will help resolve the  $a_\mu^{\text{SM}} - a_\mu^{\text{EXP}}$  discrepancy with higher confidence. To achieve this goal, E989 will record 21 times the E821 data set, while various sources of systematic uncertainties will be reduced by improved instrumentation. In this paper, an overview of the  $a_\mu$  measurement principles are presented in Section 2. The E989 experiment design and commissioning progress are described in Section 3. The current progress in Run-1 is described in Section 4.

## 2 Measurement principles

In E989, a polarized muon beam is injected into a storage ring with a uniform magnetic field. Because  $g \neq 2$  the spin precession angular velocity  $\vec{\omega}_s$  is different from the cyclotron angular velocity  $\vec{\omega}_c$ . Assuming that the magnetic field is perfectly uniform and betatron oscillations of the beam are neglected, the difference of  $\vec{\omega}_s$  and  $\vec{\omega}_c$  is [3]:

$$\vec{\omega}_a = \vec{\omega}_s - \vec{\omega}_c = -\frac{e}{m_\mu} \left[ a_\mu \vec{B} - \left( a_\mu - \frac{1}{\gamma^2 - 1} \right) \frac{\vec{\beta} \times \vec{E}}{c} \right], \quad (1)$$

where  $\vec{B}$  and  $\vec{E}$  are the magnetic and electric fields in the storage ring,  $\vec{\beta} = \vec{v}/c$  is the velocity of the muon relative to the speed of light, and  $\gamma = 1/\sqrt{1 - \beta^2}$ . In the muon storage ring a static electric field is used to focus the muon beam vertically. In order to reduce the magnitude of the  $\vec{\beta} \times \vec{E}$  term in Eq. 1, the momentum of the muon beam is chosen to be 3.094 GeV/c ( $\gamma = 29.3$ ) so that the coefficient of this term vanishes. In this experiment the *anomalous precession angular frequency*  $\omega_a$  and the average magnetic field strength  $\tilde{B}$  experienced by the muons are measured separately, and the anomalous magnetic moment is proportional to the ratio of them:

$$a_\mu = -\frac{m_\mu \omega_a}{e \tilde{B}}. \quad (2)$$

$\omega_a$  is extracted from the rate of positrons emitted in the muon decay  $\mu^+ \rightarrow e^+ \nu_e \bar{\nu}_\mu$ . Due to parity violation in weak interactions, the angular distribution of the emitted positrons is not isotropic. In the rest frame of a positive muon, high-energy positrons are more likely to be emitted along the muon spin. As the spin of the muon precesses in the magnetic field, the asymmetric angular distribution of the positrons also rotates at the angular frequency  $\omega_a$ . Because the kinetic energy of the muons in the lab frame is much higher than the rest-frame end-point energy of the emitted positrons, the positrons experience a huge Lorentz boost. Therefore, most of the positrons are emitted in the forward direction, and their lab-frame energies  $E_{lab}$  strongly depend on their emission angle  $\theta^*$  in the rest frame relative to the boost direction

$$E_{lab} \approx \gamma E^* (1 + \cos \theta^*) \quad (3)$$

where  $E^*$  is the positron energy in the rest frame of the muon. Through this mechanism,  $E_{lab}$  also oscillates at the angular frequency  $\omega_a$ . The emitted positrons have less momenta than the muons, so their orbit radius in the magnet is smaller than the muon storage orbit radius and they curve towards the inner side of the ring and eventually hit the calorimeters that measure the arrival time and energy deposition of the incoming particles. From the calorimeter readings, one can reconstruct the energy deposition versus time and extract its oscillation angular frequency (Q-method), or set a threshold on energy and reconstruct the positron count versus time and extract its oscillation angular frequency (T-method). These two methods have different systematic uncertainties, and in E989 both of them are implemented by different analysis teams, and their results will be compared and evaluated before the final result is released.

The magnetic field in the muon storage region is mapped using proton nuclear magnetic resonance (NMR) probes. The NMR system determines the free-proton precession angular frequency  $\omega_p$  which is proportional to the magnitude of the magnetic field. The average magnetic field  $\tilde{\omega}_p$  experienced by the muons is obtained by integrating the  $\omega_p$  map weighted by the measured muon distribution map. To express  $a_\mu$  in terms of  $\omega_a$  and  $\tilde{\omega}_p$ , Eq. 2 becomes

$$a_\mu = \frac{g_e m_\mu \mu_p \omega_a}{2 m_e \mu_e \tilde{\omega}_p}, \quad (4)$$

where  $g_e$  is the  $g$ -factor of an electron,  $m_\mu/m_e$  is the muon-to-electron mass ratio, and  $\mu_p/\mu_e$  is the proton-to-electron magnetic moment ratio, and these three values are already measured with uncertainties better than 22 ppb in experiments [2, 13, 14].

### 3 Overview of the E989 commissioning progress

The construction of E989 started in 2013, and in May 2017 most of the major components were built and installed. After 11 months of studying and improving the experiment, E989 was commissioned and Run-1 started at the end of March 2018. In this section, key components of the experiment will be described, together with the improvements compared to E821 and the milestones achieved during the commissioning period.

#### 3.1 Muon beam line

The muon beam [15] used in E989 is produced by the Fermilab accelerator complex. Hydrogen ions generated at the Ion Source are accelerated to 400 MeV in the Linear Accelerator and then boosted to 8 GeV in the Booster. The proton beam from the Booster is then directed to the Recycler for bunching, and then impinged on a Inconel

target to create pions. Positive pions with 3.11 GeV/c momentum are selected and directed into the Delivery Ring which was used as a part of the anti-proton source when the Tevatron was in use. Polarized muons with 3.094 GeV/c momentum are captured from forward-going pion decays. In the delivery ring, the beam goes for several turns while more pions decay into muons, and the muon bunch is separated spatially from the remaining protons so that a clean muon bunch can be extracted. The extracted muon bunches are delivered to the muon storage ring in the Muon g-2 Experiment Hall. In May 2017, all the beamlines except the Delivery Ring were commissioned. The latter was commissioned in December 2017. In the early runs from May to December 2017 protons and pions were injected together with muons into the storage ring, and since December 2017 protons and pions were eliminated before injection. Through the commissioning run, the muon beam was tuned and improved to optimize the number of muons delivered to the experiment. In May 2018, 300,000 muons per bunch were being recorded just prior to injection through the storage ring yoke, which is close to the goal set in the *Technical Design Report* [12].

### 3.2 Muon storage ring

The superconducting ring magnet provides a 1.45 T uniform magnetic field to store the muons. It is the same magnet [16] used in E821, and it was transported to Fermilab in the summer of 2013. The superconducting coils with their cryostats were transported as a whole, while the iron pieces were disassembled and transported separately and then reassembled. The magnet was successfully cooled and powered in 2015, and since then procedures for operating the magnet safely and stably were developed.



Figure 2: The photo of the storage ring magnet and its cross-sectional view. The circular region between the poles represents the muon storage region. The magic radius of  $\rho=7112$  mm relative to the center of the ring is labeled. The superconducting coils are marked by the rectangles at the inner and outer radii.

The cross-section of the storage ring magnet is shown in Figure 2. The magnetic field points vertically upwards in the space between the pole pieces. To achieve a better uncertainty on  $\tilde{\omega}_p$ , the magnet has to be shimmed to a higher uniformity than that was the case in E821. In the magnet shimming campaign of E989, each of the adjustable iron pieces (top/bottom hats, pole pieces, edge shim and wedge shims) was adjusted carefully to reduce the transverse (radial and vertical directions) and longitudinal (azimuthal direction in the ring) gradients of the field. To shim the non-uniformity at even shorter scales than the sizes of these iron pieces, customized iron foils were used to increase the field strength where the field was weak.  $\sim 8500$  precisely cut iron foils were epoxied to the surface of the pole pieces. It took 10 months to finish the shimming, and the peak-to-peak variation of the field reached  $\pm 25$  ppm in the azimuthal direction and  $\pm 4$  ppm in the transverse directions [17]. Besides these passive shimming techniques, 200 concentric coils are placed on the surface of the pole pieces, and the current in the coils are programmable in order to cancel the remaining transverse field non-uniformity. After optimizing the current in the coils, the peak-to-peak variation of the azimuthally averaged field cross-sectional map was reduced to 2.5 ppm. The current in the main magnet coils can be actively adjusted based on the field measurements by the fixed probes. This feedback mechanism maintains the field at a constant value over a long time period.

Twelve sections of the storage ring vacuum chamber inherited from E821 were cleaned and installed by March 2017. Some chambers were modified to host new devices like the in-vacuum straw trackers. Inside the vacuum chamber all around the ring, there are rails guiding the magnetic field scanning device. Because the rails determine the radial and vertical coordinates of the field scanner, the positions and shapes of rails in each chamber section were aligned at the sub-millimeter level.

The muon beam enters the magnet through an aperture in the back of the iron yoke. From the inner edge of the iron yoke to the edge of the pole pieces, the magnetic field increases from near zero to the full field strength. To prevent the beam from being deflected by the main field before reaching the storage region, a superconducting magnet called the *inflector* is used to cancel the main magnetic field along the path of the muon beam between the cryostat of the outer magnet coils and the storage ring vacuum. It has a superconducting shield so that the field generated by the inflector currents does not affect the highly uniform field in the beam storage region. The inflector used in E821 was installed and has been operated since December 2016. A new inflector magnet with an open-ended design is being built for FY20 running. The open-ended inflector does not scatter muons at the exit and so will improve the muon storage efficiency.

When the muons exit the inflector they are displaced radially 77 mm outward from the central (ideal) orbit of the storage ring, and therefore after injection the muon orbit is a circle offset by the same amount from the ideal orbit. The muons cross the ideal orbit approximately  $90^\circ$  azimuthally downstream from the end of the inflector.

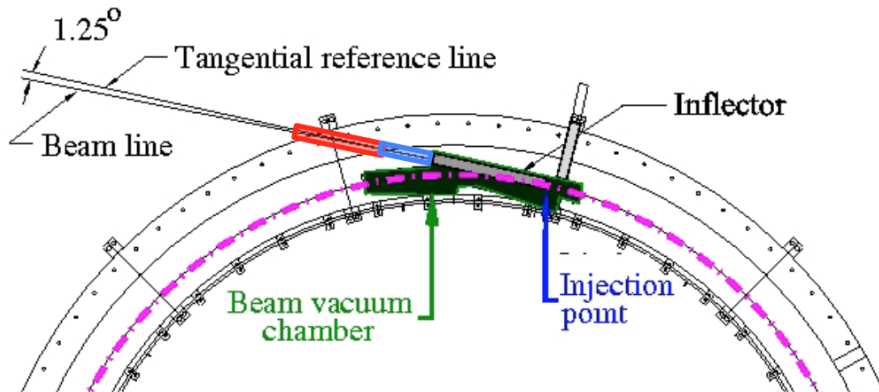


Figure 3: Schematics of the muon beam entering the storage ring through the tunnel in the iron and then the inflector.

At this point, the direction of the muons are not tangential to the ideal orbit. The kicker magnet imposes a fast magnetic field pulse to the incoming muon bunch, and bends them onto the ideal orbit. There are three kickers in the E989 storage ring, and each of them is a pair of metal plates on the inner and outer radius of the beam. A  $\sim 5000$  A current is conducted through the plates creating a transient vertical field peaked at  $\sim 250$  Gauss. The ideal pulse shape of the kicker is square with a flat top that lasts for  $\sim 100$  ns. This ideal pulse was not achieved during the commissioning run and significant work was undertaken to improve the characteristics of the pulse and a larger kicker pulse will be available in the upcoming FY19 run.

Electrostatic quadrupoles are used in the storage ring to confine the muon beam vertically, and they cover  $\sim 43\%$  of the total circumference. The electrodes from E821 were polished, aligned and installed into the vacuum chambers early in 2017. The electrodes are aluminum plates. When the muon beam moves from the inflector to the kicker for the first time, it passes through the outer electrode. In E989 this electrode is made of aluminized mylar in order to reduce the beam scattering and thus improve the beam storage efficiency. Because of the variance in the muon momentum, not all muons are at the *magic momentum* and a small correction must be applied to  $\omega_a$ . The positions of the electrodes are surveyed to the sub-millimeter level and the electric field generated by the electrodes are modeled by Opera3D. The electrodes are designed to be operated up to 25 kV. Dedicated procedures have been developed to condition the electrodes and to date data has been taken with potentials between 15 and 21 kV.

### 3.3 Detector system

Twenty-four calorimeter stations are evenly distributed along the storage ring on the inner side of the vacuum chamber. Decay positrons exit the vacuum chamber through its aluminum wall and immediately enter the  $\text{PbF}_2$  crystals of the calorimeters. The high-energy positron generates a shower of Cherenkov light in the crystal, and the number of photons are proportional to the energy of the primary positron. At the end of each crystal the Cherenkov photons are detected by a silicon photomultiplier (SiPM), and the signal from the SiPM is amplified and then read out by a 800-MSPS 12-bit waveform digitizer. Each calorimeter station has a  $6(\text{V}) \times 9(\text{H})$  array of crystals. Signals from all crystals are continuously digitized for  $700 \mu\text{s}$  after the trigger signal synchronized to the incoming muon bunch. For the T-method, to reduce the data size written to the disk, only the waveform section near a SiPM signal pulse is saved. The pulse finding algorithm is implemented using Graphic Processor Units (GPU). The multiplicities and positions of the particles hitting a calorimeter station can be determined by the topology of the trigger pattern and the signal amplitude distribution. Pileup pulses separated larger than  $\sim 4 \text{ ns}$  are also resolvable in the E989 calorimeters. The gain stability of each SiPM is monitored using a dedicated laser-calibration system [18]. The response of the calorimeter system was thoroughly characterised in two SLAC testbeams. The calorimeter stations together with the laser calibration system, data acquisition system and slow control system was finished before May 2017.

Charged particle straw tracking detectors [19] were designed to reconstruct the trajectories of positrons before they enter the calorimeters. One tracker station was constructed and commissioned in May 2017, and a second tracker station was commissioned in December 2017. Each tracker station comprises of 8 modules, and each module has two planes of straws oriented at  $7.5^\circ$  with respect each other, so that both the horizontal and vertical coordinates of the trajectory can be determined. The straws are made of  $15\text{-}\mu\text{m}$  thick aluminized mylar foils with a gold-plated tungsten wire ( $d=25 \mu\text{m}$ ) at the center. Each straw is filled with an Argon-Ethane(50%) gas mixture. A resolution of  $165 \mu\text{m}$  in plane perpendicular to the straw has been achieved. Tracks are extrapolated forward to match with the calorimeter and to the point of tangency of the ideal muon orbit allowing the profile of the beam distribution to be determined.

There are also 3 more detector systems used to measure the muon beam. The T0 detector is a scintillator with two photomultiplier tubes. It is placed at the end of the delivery beam line before the muons enters the magnet yoke. It gives the time when the muon bunch arrives, and this timing information is important for tuning the kicker timing. The integrated pulse amplitude of the T0 signal is also a good proxy for the total number of muons in that bunch. The inflector beam monitors (IBMS) are scintillator fiber arrays in the muon beam near the inflector. Two IMBS detectors are



commissioned. They are located upstream from the inflector at atmosphere, providing beam profiles and positions before the muons entering the inflector. Inside the muon storage ring, there are also two stations of scintillation fiber detectors for profiling the muon beam. They are useful for studying the beam dynamics, but destructive for the muon beam. During production runs, the scintillation fiber detectors in the muon storage ring are extracted from the beam storage region.

### 3.4 Magnetic field measurement system

The magnetic field in the muon storage region is scanned by a trolley that moves on the rails inside the vacuum chamber, which carries 17 NMR probes and the electronics for digitizing the NMR waveform. The trolley is pulled by two cables on each side to move, and the cables are wound on motorized drums. One of the cables is also the signal cable for the NMR electronics. The trolley shell was the one used in E821 [3]. The motion control is fully automated and the new NMR electronics allows raw NMR waveforms to be stored and analysed. The muon beam is turned off during the magnetic field scanning. During normal runs with the muon beam, the trolley is extracted from the storage region but still stays inside the vacuum chamber. During the stable run period two field scans were performed per week.

There are 378 NMR probes installed at fixed locations around the ring to monitor the drift of the magnetic field [17]. They are installed in grooves on the vacuum chambers, above and below the muon storage region. The readings from these fixed probes are used to predict the field in the muon storage region, and also used for the current feedback mechanism to maintain a stable field. The NMR probes for the trolley and fixed probe systems use petroleum jelly as the detection material. They were designed and built before 2015, used in the shimming campaign in 2016 and then installed and commissioned in 2017. The electronics system for the fixed probes was installed and commissioned in May 2017, and then several significant upgrades were implemented from July to December in 2017. The NMR frequency extraction algorithm is also implemented on GPUs, and the total time for reading and analyzing waveforms from all fixed probes is 1.67 s, compared to  $\sim 10$  s in E821.

The magnetic field read by the NMR probes carried by the trolley is perturbed by the material of the trolley shell and electronics, and the material itself is also magnetized in the field. Because the protons in the NMR probes are in molecules, their NMR frequency is proportional to, but different from, the free proton NMR frequency. To correct for these effect, we built a cylindrical probe with pure water as the detection material. This probe has a well-known magnetic susceptibility and chemical shift [14]. The perturbation of the probe itself was measured. Each NMR probe on the trolley has to be calibrated to this calibration probe, and dedicated calibration runs were conducted in vacuum. Spherical calibration probes using water and  $^3\text{He}$  as the detection material have also been fabricated. These calibration probes

will be cross-calibrated to perform a consistency check.

## 4 The Run-1 Physics Data Accumulation

The commissioning run from May 2017 to July 2017 allowed the performance of the beamline, injection and detector systems to be evaluated. The characteristic signature of  $\omega_a$  was observed in the data, but the muon storage efficiency was significantly below the design. Throughout the summer and with the first beam in November 2017 considerable optimisations and improvements were implemented and the first physics quality run, Run-1, commenced at the end of March 2018.

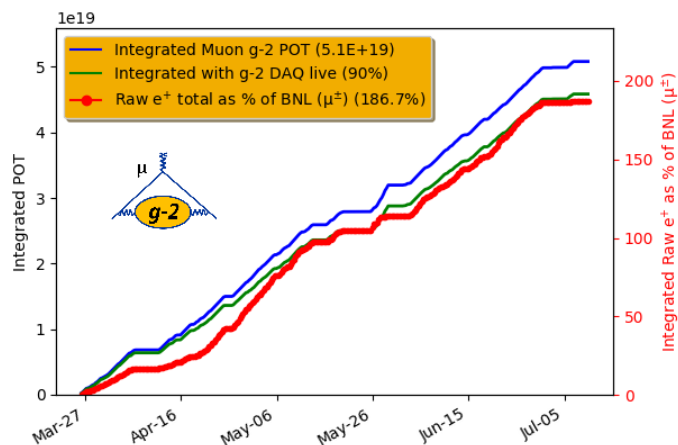


Figure 4: Integrated numbers of proton-on-target and the raw number of detected decay positrons recorded during Run-1.

A dataset exceeding that accumulated by E821 was collected before the end of May 2018. During stable running approximately 500 decay positrons per circulating muon bunch were recorded. The data acquisition system recorded data at up to 250 Mb/sec and was live for  $\sim 90\%$  of the beam-on time. The storage ring magnet was operational over 95% of the time and more than 30 magnetic field scans were successfully conducted. The reference clock frequency was blinded for the duration of the Run-1 period. The full analysis of this Run-1 dataset is expected to be completed in the second half of 2019.

In Run-1, the number of stored muons was approximately 50% of the design and a number of factors have been identified to increase the number of stored muons towards the design goal and particularly to improve the momentum variance of the beam. Upgrades to the kicker and electric quadrupole systems will be undertaken during the summer of 2018 ready for the start of the next physics data taking period in November 2018. In addition fiber-glass insulation and improved air conditioning

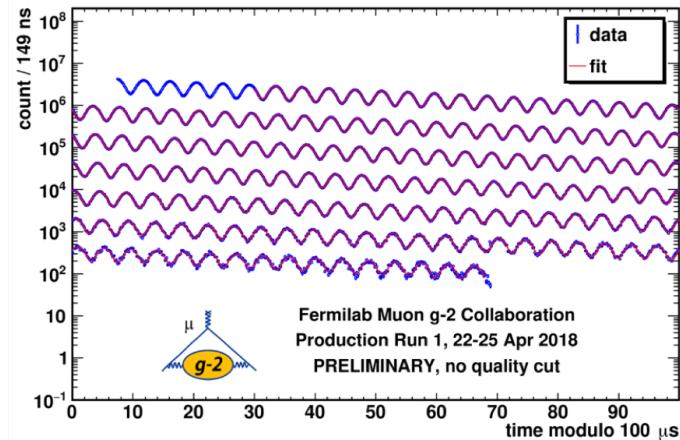


Figure 5: (PRELIMINARY) Positron counting rate spectrum fitted to  $N_0 \exp(-t/\tau)(1 + A \cos(\omega_a t + \phi))$ . No quality controls are implemented.

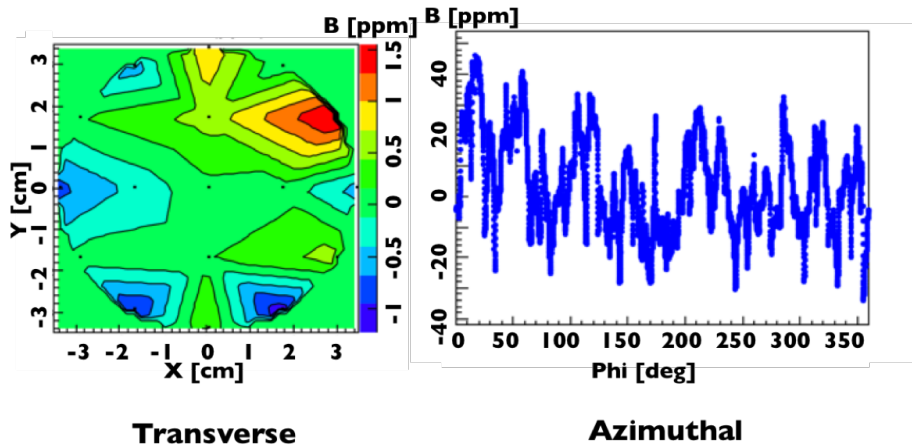


Figure 6: (PRELIMINARY) Magnetic field map scanned on May 16th 2018. The transverse magnetic field distribution is averaged over the azimuthal direction, while each data point in the azimuthal magnetic field distribution is averaged in the transverse direction. No calibration, drift correction and quality controls are implemented.

will be installed to ensure that temperature fluctuations in the experimental hall are reduced which in turn reduces the variance in the magnetic field and calorimeter gain.

A higher power air conditioning system in the experiment hall will maintain the temperature better and thus reduce the drift of the magnetic field and the detector gains. Fiberglass insulation will also be installed onto the magnet to achieve higher magnetic field stability.

## 5 Conclusion

The Muon  $g-2$  experiment E989 has been successfully commissioned and a Run-1 dataset exceeding the statistics of the E821 experiment has been accumulated. The goal of this experiment is to search for beyond-SM physics by measuring the anomalous magnetic moment  $a_\mu$  of muons with an uncertainty better than 140 ppb. The Run-1 analysis is expected to measure  $a_\mu$  with an uncertainty similar to that of E821. A dataset several times the size of E821 will be accumulated in 2019 with significant improvements in the muon storage efficiency and beam quality.

## ACKNOWLEDGEMENTS

We thank David Flay, Erik Swanson, Hogan Nguyen, Jason Crnkovic, Chris Stoughton, Jarek Kaspar, David Hertzog, and Jason Hempstead for their expert knowledge about each system of the muon  $g-2$  experiment. We thank the Fermilab management and staff for their strong support of this experiment.

The Muon  $g - 2$  experiment was performed at the Fermi National Accelerator Laboratory, a U.S. Department of Energy, Office of Science, HEP User Facility. Fermilab is managed by Fermi Research Alliance, LLC (FRA), acting under Contract No. DE-AC02-07CH11359. Additional support for the experiment was provided by the Department of Energy offices of HEP and NP (USA), the National Science Foundation (USA), the Istituto Nazionale di Fisica Nucleare (Italy), the Science and Technology Facilities Council (UK), the Royal Society (UK), the European Union's Horizon 2020 research and innovation programme under the Marie Skłodowska-Curie grant agreements No. 690835 (MUSE), No. 734303 (NEWS), MOST and NSFC (China), MSIP and NRF (Republic of Korea).

## References

- [1] Julian Schwinger. On quantum-electrodynamics and the magnetic moment of the electron. *Phys. Rev.*, 73:416–417, Feb 1948.
- [2] D. Hanneke, S. Fogwell, and G. Gabrielse. New measurement of the electron magnetic moment and the fine structure constant. *Phys. Rev. Lett.*, 100:120801, Mar 2008.
- [3] G. W. et. al. Bennett. Final report of the e821 muon anomalous magnetic moment measurement at bnl. *Phys. Rev. D*, 73:072003, Apr 2006.

- [4] Peter Cox, Chengcheng Han, and Tsutomu T. Yanagida. Muon  $g - 2$  and dark matter in the minimal supersymmetric standard model. *Phys. Rev. D*, 98:055015, Sep 2018.
- [5] Alexander Keshavarzi, Daisuke Nomura, and Thomas Teubner. Muon  $g - 2$  and  $\alpha(M_Z^2)$ : A new data-based analysis. *Phys. Rev. D*, 97:114025, Jun 2018.
- [6] Friedrich Jegerlehner. *The Anomalous Magnetic Moment of the Muon*, volume 274 of *Springer Tracts in Modern Physics*. Springer, 2017.
- [7] Michel Davier. e+e results from babar and implications for the muon g-2. *Nuclear Physics B - Proceedings Supplements*, 253-255:123 – 126, 2014. The Twelfth International Workshop on Tau-Lepton Physics (TAU2012).
- [8] Thomas Blum, Norman Christ, Masashi Hayakawa, Taku Izubuchi, Luchang Jin, Chulwoo Jung, and Christoph Lehner. Using infinite-volume, continuum qed and lattice qed for the hadronic light-by-light contribution to the muon anomalous magnetic moment. *Phys. Rev. D*, 96:034515, Aug 2017.
- [9] Harvey B. Meyer and Hartmut Wittig. Lattice QCD and the anomalous magnetic moment of the muon. 2018.
- [10] Gilberto Colangelo, Martin Hoferichter, Massimiliano Procura, and Peter Stoffer. Dispersion relation for hadronic light-by-light scattering: two-pion contributions. *Journal of High Energy Physics*, 2017(4):161, Apr 2017.
- [11] Martin Hoferichter, Bai-Long Hoid, Bastian Kubis, Stefan Leupold, and Sebastian P. Schneider. Pion-pole contribution to hadronic light-by-light scattering in the anomalous magnetic moment of the muon. *Phys. Rev. Lett.*, 121:112002, Sep 2018.
- [12] J. Grange et al. Muon (g-2) Technical Design Report. 2015.
- [13] W. et. al. Liu. High precision measurements of the ground state hyperfine structure interval of muonium and of the muon magnetic moment. *Phys. Rev. Lett.*, 82:711–714, Jan 1999.
- [14] Peter J. Mohr, David B. Newell, and Barry N. Taylor. Codata recommended values of the fundamental physical constants: 2014. *Rev. Mod. Phys.*, 88:035009, Sep 2016.
- [15] Diktys Stratakis, Mary E. Convery, Carol Johnstone, John Johnstone, James P. Morgan, Dean Still, Jason D. Crnkovic, Vladimir Tishchenko, William M. Morse, and Michael J. Syphers. Accelerator performance analysis of the fermilab muon campus. *Phys. Rev. Accel. Beams*, 20:111003, Nov 2017.

- [16] G.T. Danby and et. al. The brookhaven muon storage ring magnet. *Nuclear Instruments and Methods in Physics Research Section A: Accelerators, Spectrometers, Detectors and Associated Equipment*, 457(1):151 – 174, 2001.
- [17] Matthias W. Smith. *Developing the Precision Magnetic Field for the E989 Muon  $g-2$  Experiment*. PhD thesis, University of Washington, Seattle, 2017.
- [18] A. Anastasi et. al. Test of candidate light distributors for the muon ( $g2$ ) laser calibration system. *Nuclear Instruments and Methods in Physics Research Section A: Accelerators, Spectrometers, Detectors and Associated Equipment*, 788:43 – 48, 2015.
- [19] Thomas Simon Stuttard. *The development, testing and characterisation of a straw tracking detector and readout system for the Fermilab muon  $g-2$  experiment*. PhD thesis, University College London, 2018.